

Explore the Wavelength-dependent Generation of Reactive Species in the Photocatalytic Process

Peng Zhang^{1,2}, Cheng Peng^{1,#}, Hui Li¹, Jing Huang¹, Yan Wang¹, Youqing Yu³, Shimin Ding³,
Songli Liu^{1,*}, Yanchun Zhao¹

¹ College of Materials Science and Engineering, Yangtze Normal University, Chongqing
408100, China

² Helmholtz-Zentrum Berlin for Materials and Energy, Institute of Applied Materials, Berlin
14109, Germany

³ Green Intelligence Environmental School, Yangtze Normal University, Chongqing 408100,
China

Corresponding author. E-mail: 20090008@yznu.edu.cn

* Corresponding author. E-mail: lsli@yznu.edu.cn

Abstract: Reactive species, such as the hydroxyl radical ($\cdot\text{OH}$), holes (h^+), and superoxide radicals ($\cdot\text{O}_2^-$), are considered the main active substances involved in the photocatalytic degradation of organic pollutants. However, to the best of our knowledge, the effect of the photon energy on the generation of these species has never been examined in detail. In this study, the production of $\cdot\text{OH}$ radicals, holes, and $\cdot\text{O}_2^-$ radicals, using Nb_2O_5 , in the photocatalytic process is observed as a function of the excitation wavelength. The ESR results clearly show that all three active species can be created at 355 nm using both pure and C-doped Nb_2O_5 . At 532 nm, which is well beyond its absorption edge (399 nm), however, only h^+ and $\cdot\text{O}_2^-$ radicals are produced for pure Nb_2O_5 , while all three species can be produced using C-doped Nb_2O_5 . The results of the trapping experiments suggest that $\cdot\text{O}_2^-$ and h^+ are the main reactive species, which are responsible for the photocatalytic degradation. The photogenerated holes play a crucial role in the wavelength range of 365-420 nm but become less active with increasing wavelength. $\cdot\text{O}_2^-$ shows little wavelength dependence and is consistently active at all wavelengths between 365 and 630 nm - especially with C-doped Nb_2O_5 . Overall, it can be concluded that the presence of localized states within the forbidden gap has a profound impact on the photocatalytic activity in the visible-wavelength region.

Keywords: Photogenerated carriers; Reactive species; Wavelength dependence; Localized

1 Introduction

The process of photocatalysis involves three steps: light absorption, charge generation/transportation, chemical catalysis [1-3]. Upon absorption of photons with energies larger than the bandgap of the semiconductor, photogenerated electrons are excited from the valence band to the conduction band, and they leave holes in the conduction band. Unfortunately, there is a barrier for the widespread application of photocatalytic methods: most semiconductors show little light-absorption in the visible region due to their relatively large bandgaps. It is generally believed that wide-bandgap semiconductor photocatalysts such as TiO_2 [4] can only work with UV light, while narrow-bandgap semiconductor photocatalysts such as g- C_3N_4 [5] and Bi_2WO_6 [6] can only respond to a small portion of visible light. The utilization of the long-wavelength spectrum (> 600 nm), which accounts for over 40 % of solar energy, is indeed crucial to improve solar conversion efficiencies [7]. Much effort has been devoted to extend the light absorption of different semiconductors using defect engineering [8, 9], metal doping [9, 10], nonmetal doping [9, 11], ect. Among these approaches, nonmetal doping is a novel and promising strategy to expand the light absorption from the UV into the visible region. This is because the impurity states of non-metal dopants are generated above the valence band.

Notably, in addition to the band-to-band absorption (similar to defect-free crystalline semiconductors), an amorphous structure with quantum fluctuations within the lattice can push extended electronic states into the empty gap region to form a tail state. This can produce Urbach-tail absorption, which creates the possibility to harvest a broader part of the solar spectrum [12-14]. The mediation of mid-gap states, which results from amorphization, is responsible for efficient carrier separation and the slightly prolonged carrier lifetime. This is crucial to improve photocatalytic activity [13]. However, some researchers stated that these localized states in the bandgap can trap the photoinduced carriers, which leads to effective charge recombination during photocatalytic reactions [15]. More importantly, the defect-induced localized states were found to weaken the photo-generated carriers' oxidation- and reduction-capacities in anatase TiO_2 [16]. Hence, the suppression of the defect states in semiconductors was proposed to optimize the photocatalytic performance of several photocatalysts.

In this study, the production of $\cdot OH$ radicals, holes, and $\cdot O_2^-$ radicals, using Nb_2O_5

in the photodegradation process, was monitored as a function of the excitation wavelength. The prepared carbon-doped Nb₂O₅ as well as the reference pure Nb₂O₅ were analyzed using several analytical characterization techniques to investigate the crystalline structures, morphology, chemical composition, and optical properties. In order to understand the transfer pathway of photogenerated carriers in both pure and carbon-doped Nb₂O₅, ESR spectra were measured with monochromatic laser irradiation to record the generation of reactive species (including ·OH radicals, holes, ·O₂⁻ radicals). Trapping experiments were also performed using pure and carbon-doped Nb₂O₅ and irradiation with four different monochromatic LEDs (to trap the produced reactive species in photodegradation of MB). We found that carbon doping not only reduces the bandgap energy of the material but also shifts the conduction band as well as the localized states in the forbidden gap upward. Due to the localized states, the absorption of photons can also occur for photon energies lower than the bandgap, which leads to the wavelength-dependent production of reactive species during the photocatalytic process. The obtained results suggest the presence of localized states in the forbidden gap has a profound impact upon the photocatalytic activity in the visible region.

2 Experimental

2.1 Material and reagents

Niobium oxalate hydrate [C₁₀H₅NbO₂₀], poly (vinyl pyrrolidone) (PVP), methylene blue (MB), disodium ethylenediamine tetra-acetic acid (EDTA-2Na), benzoquinone (BQ), 5,5-dimethyl-1-pyrroline N-oxide (DMPO), ammonium oxalate (AO), 2,2,6,6-tetramethylpiperidine-1-oxyl (TEMPO), tert-butyl alcohol (TBA), and isopropanol (IPA) were purchased from Aladdin Reagent (Shanghai, China). All chemicals were of analytical grade and used as received without further purification.

2.2 Synthesis of the catalysts

2.2.1 Synthesis of Nb₂O₅ nanoparticles

In a typical preparation, 1.076 g C₁₀H₅NbO₂₀ was dissolved in 30 mL of distilled water during stirring at 60 °C for 30 min until the solution became clear. The transparent solution was then sealed into a 50 mL Teflon-lined autoclave and heat-treated at 180 °C for 24 h. After the reaction had finished, the precipitate was collected using centrifugation and washed repeatedly with distilled water. Subsequently it was

dried in an oven at 90 °C for 24 h. The obtained powder was marked as 180NO. Finally, the powder was annealed for 40 min at a temperature of 300 °C in a tubular annealing furnace, and the obtained product was referred to as 300NO.

2.2.2 Synthesis of C-doped Nb₂O₅ nanoparticles

Typically, 1.076 g C₁₀H₅NbO₂₀ was dissolved in 25 mL of distilled water, while stirring at 60 °C for 30 min until the solution became clear. This yielded solution A. 0.2 g PVP was dissolved in 5 mL of distilled water to form solution B. Solution B was slowly dropped into solution A and stirred for 10 min and then hydrothermally treated at 180 °C for 24 h. After the reaction was finished, the precipitate was collected using centrifugation, washed repeatedly with distilled water, and dried in an oven at 90 °C for 24 h. The obtained powder was referred to as 180NO-PVP. The powder was further annealed at 300 °C in air for 40 min, and the obtained product was named 300NO-PVP.

2.3 Characterization

Powder X-ray diffraction (XRD) patterns were recorded in the $20^\circ \leq 2\theta \leq 70^\circ$ range using a Bruker D8 Advance diffractometer. The microstructures were investigated using a cold field scanning electron microscope (FE-SEM, Hitachi S4800, Japan). The X-ray photoelectron spectroscopy (XPS) was performed using a Thermo Scientific VG ESCALAB 250Xi photoelectron spectrometer with the Al K α Line as excitation source and an energy step of 0.1 eV. The nitrogen adsorption-desorption measurements were conducted at 77.35 K using a Micromeritics ASAP 2460 surface area and porosity analyzer (Micromeritics Instrument Corporation). Each sample was degassed at 200 °C for 10 h prior to the adsorption and desorption measurements. The UV-visible diffuse reflectance spectra were recorded on a UV/Vis NIR scanning spectrophotometer (Hitachi, UV-4100) ranging from 200 to 800 nm. The steady-state photoluminescence spectra and time-resolved transient photoluminescence spectra were measured using an Edinburgh FLS980 fluorescence spectrophotometer with the 325 nm line of a Xe lamp as excitation source. The electrochemical measurements were carried out on a CHI 760E electrochemical workstation (Shanghai, China) using a three-electrode system. ESR spectra were measured with a Bruker model JEOL JES FA200 spectrometer with 355 nm and 532 nm laser irradiation, respectively. 5,5-dimethyl-1-pyrroline N-oxide (DMPO) was selected as the spin trap for the detection of the hydroxyl ($\cdot\text{OH}$) and superoxide ($\cdot\text{O}_2^-$) radicals, and 2,2,6,6-tetramethylpiperidine-1-oxyl (TEMPO) was used to characterize photogenerated holes.

2.4 Adsorption experiments

In a typical procedure, 20 mg photocatalyst was dispersed in 50 mL MB solution (50 ppm), and the suspension was stirred, magnetically, in the dark. 4 mL of the MB solution was sampled at certain time intervals, and the concentration was determined by monitoring its characteristic absorption at 664 nm using a UV-Vis spectrophotometer (Rigol Ultra-6100). The adsorption efficiency could be calculated with the following equation: $D\% = (C_0 - C_t) / C_0 * 100$, where C_0 and C_t denote the initial and equilibrium concentrations of MB at times 0 and t, respectively, where t is the irradiation time.

2.5 Trapping experiments

Trapping experiments were performed using a PCX50A Discover multi-channel parallel photocatalytic reaction system. These were done to characterize the wavelength-dependent reactive species produced during the photodegradation of MB. A white-light LED ($400 \text{ nm} \leq \lambda \leq 800 \text{ nm}$) and four monochromatic LEDs (365 nm, 420 nm, 535 nm, and 630 nm) with the same output power (5W) were used as light sources in the trapping experiments. Both Iso-propyl alcohol (IPA) and tert-butyl alcohol (TBA) were used as scavengers to capture the hydroxyl radicals ($\cdot\text{OH}$) [17, 18]. Ethylenediaminetetraacetic acid disodium (EDTA-2Na) and ammonium oxalate (AO) were used to quench holes (h^+) [19, 20]. Benzoquinone (BQ) was used as capture agent for the superoxide anion radical ($\cdot\text{O}_2^-$) [21]. In a typical procedure, 50 mL of MB solution (50 ppm), a certain amount of scavenger, and 20 mg of the photocatalyst were placed into a 50 mL bottle with a cap. Then, the photocatalytic reaction was carried out immediately. A 4.0 mL aliquot was separated at regular intervals (20 min), and the concentration was determined using a Rigol Ultra-6100 UV-Vis spectrophotometer.

3 Results and discussion

3.1 Characteristics and properties of pure Nb_2O_5 and C-doped

Nb_2O_5

XRD was used to determine the crystalline phase of pure Nb_2O_5 and C-doped Nb_2O_5 nanoparticles - see Fig. 1. The diffraction peaks of Nb_2O_5 at 2θ values of 22.73° and 46.40° correspond to the (001) and (002) planes of pseudo-hexagonal Nb_2O_5 (JCPDS card No. 28-0317), respectively. The weak and wide diffraction peaks suggest low crystallinity. The diffraction peaks associated with the other facets, e.g.,

(100), (101), (110), and (102), seem to be lost in the background due to very low intrinsic intensity. The sample 300NO, which was obtained by calcination of 180NO in air at 300 °C for 40 min, displays a similar XRD pattern as 180NO - except that the intensity of the diffraction peaks increased. 180NO-PVP and 300NO-PVP also display a similar XRD pattern as 180NO. These results suggest that PVP capping or calcination at 300 °C for 40 min did not significantly affect the crystal structure of Nb₂O₅ nanoparticles.

As shown in Fig.2, the morphologies of the photocatalysts were investigated using scanning electron microscopy (SEM). In Fig.2a, the hydrothermally synthesized Nb₂O₅ nanoparticles (180NO) show a high degree of agglomeration, and most large particles are in fact agglomerates of much smaller particles. Many cavities can be clearly observed between the agglomerates, which can be considered an important parameter that affects the adsorption of the photocatalysts. All other Nb₂O₅ samples, including calcined Nb₂O₅ (300NO) and PVP modified Nb₂O₅ (180NO-PVP and 300NO-PVP), exhibit similar morphologies as pure Nb₂O₅ (180NO) - see Figs.2b, 2c, and 2d. The result indicates that neither calcination nor PVP modification had any clear effect on the morphology of Nb₂O₅ nanoparticles.

The N₂ adsorption-desorption isotherms and the pore diameter distribution curves of pure Nb₂O₅ and C-doped Nb₂O₅ are shown in Figs. 3a and 3b, respectively. The distinct hysteresis loop for all four samples in Fig. 3a can be categorized as a type IV isotherm [22], which is a typical isotherm for mesoporous materials. The BET specific surface areas were calculated as 224.24 and 219.12 m²·g⁻¹ for 180NO and 300NO, respectively. Interestingly, 300NO-PVP (248.19 m²·g⁻¹) exhibits a much higher BET surface area than 180NO-PVP (200.39 m²·g⁻¹). The pore-size distribution curves in Fig. 3b indicate that all the four samples mainly show a pore-size distribution ranging from 1 to 30 nm. This also confirms the presence of mesoporous features. The average pore diameter of the samples 180NO, 300NO, 180NO-PVP, and 300NO-PVP were measured to be 5.87, 6.72, 6.28, and 6.89 nm, respectively.

XPS spectra of 300NO and 300NO-PVP are shown in Fig.4. For the Nb 3d spectrum (Fig. 4a) of 300NO, two peaks, which centered at binding energies of 207.3 eV and 210.1 eV, could be assigned to Nb 3d_{5/2} and Nb 3d_{3/2}, respectively, and resulted from the Nb spin-orbital doublet, in good agreement with those of Nb₂O₅ [23-25]. Compared with pure Nb₂O₅, a weak peak at 208 eV appeared in the XPS spectrum of the 300NO-PVP sample, which could be assigned to the Nb(3+)-O bond [26, 27]. No obvious Nb-C signal was observed in the XPS spectrum of 300NO-PVP. Note that the

intensity of Nb-C bond at about 203.9 eV was very low, even in the spectra of Nb₂CT_x MXene and the NbC powder [23, 26, 27]. The C1s spectra of 300NO and 300NO-PVP are similar (Fig. 4b). The three main peaks, which are located at 284.8, 286.4, and 288.9 eV, can be assigned to graphitic carbon C-C, CH_x, and O-C=O bonds, respectively [21, 24-28]. In Fig.4c, the O 1s spectra of both 300NO and 300NO-PVP can be deconvoluted into two peaks (530.2 and 532.1 eV), which correspond to the oxygen anion Nb-O bond in Nb₂O₅ and surface oxygen, respectively [24, 29].

Furthermore, valence band XPS (VB-XPS) was performed to determine the VB positions of 300NO and 300NO-PVP. As shown in Fig. 4d, by extrapolating the intersection of the tangent to the baseline of the VB-XPS curve, the VB edge energy (E_{VB}) of 300NO was found to be 2.85 eV (vs. NHE). For the 300NO-PVP sample, the valence band position shifted by about 0.25 eV, towards higher energy (2.60 eV vs. NHE), compared to 300NO. According to the results above, we can conclude that the red shift is due to C doping. The same trend is also true for other C-doped semiconductors, including ZnO [30, 31] and TiO₂ [32-34]. On the other hand, some new localized electronic states, which are typical for doped crystalline semiconductors and many amorphous semiconductors [12, 35-37], were observed above the valence band edge in both 300NO and 300NO-PVP - see Fig. 4d.

UV-Vis absorption spectra were carried out to study the light response of pure Nb₂O₅ and C-doped Nb₂O₅ photocatalysts. As shown in Fig.5a, the absorption edge of samples 180NO and 300NO were located at 397 and 399 nm, respectively, which suggests poor visible-light-harvesting capabilities. As for 180NO-PVP, a slight redshift at the absorption edge (407 nm) was achieved compared to sample 180NO. In particular, the C-doped 300NO-PVP exhibits remarkably improved light absorption, especially in the visible-light region, and its absorption range extends even above 800 nm, which indicates a broad-spectrum response-characteristic. The bandgaps of the samples can be estimated from the UV-vis absorbance spectra using the Kubelka-Munk equation. As shown in Fig.5b, the calculated bandgaps of all samples, 180NO, 300NO, 180NO-PVP and 300NO-PVP were 3.34 eV, 3.32 eV, 3.29 eV, and 2.99 eV, respectively. The result suggests that C doping can induce clear bandgap-narrowing compared with pure Nb₂O₅. As a consequence, the absorption spectra of the C-doped Nb₂O₅ were widened and the overall light-absorption efficiency could be enhanced, which is consistent with the observed color change of the samples (from white to yellow). It is, thus, possible to enhance the photocatalytic activity of Nb₂O₅ through C doping.

The PL spectra of samples 300NO and 300NO-PVP are shown in Fig. 6a. Clearly, the fluorescence of 300NO-PVP is significantly lower than that of 300NO, which suggests successful suppression of the recombination of photogenerated charge-carriers via C-doping. Time-resolved photoluminescence decay spectra were also measured – see Fig. 6b. The lifetimes of 300NO and 300NO-PVP were 3.7 and 4.1 ns, respectively. The longer lifetime of intrinsic fluorescence (for C-doped Nb₂O₅) suggests a reduction in the radiative recombination of charge carriers compared to pure Nb₂O₅. Photoelectrochemical measurements, including transient photocurrent analysis and electrochemical impedance spectroscopy, were also conducted to study the charge transfer efficiency. Fig.6c shows the photocurrent densities of 300NO and 300NO-PVP for visible-light irradiation. Pure Nb₂O₅ (300NO) generated a relatively low current-density. Compared to 300NO, the current density of 300NO-PVP can be substantially increased (about 100%), which suggests a higher separation- and transfer-efficiency of photogenerated charge-carriers. The transfer and recombination abilities of photogenerated electron-hole pairs of the photocatalysts could also be investigated using the electrochemical impedance spectra (EIS). Fig. 6d shows that the arc radius of 300NO-PVP was smaller than for 300NO. This suggests that the C-doped Nb₂O₅ (300NO-PVP) has a higher photoinduced electrons-transfer efficiency.

The MB adsorption (as a function of adsorption time) for different photocatalysts was measured – see Fig. 7. The obtained results indicate that these Nb₂O₅ nanoparticles were very good adsorbents to facilitate MB elimination from aqueous solutions (as a result of their high specific surface area and mesoporous structures). Moreover, 300NO showed the highest removal efficiency for MB (almost 100%), which was achieved after 240 min. Both 180NO and 300NO displayed a higher adsorption capacity than 180NO-PVP and 300NO-PVP. A slightly lower adsorption capacity was achieved for 180NO compared to 300NO, which indicates that the calcination at 300 °C for 40 min did not significantly affect the mesoporous structure of the material. The same conclusion can be drawn after comparing the adsorption capacity of 180NO-PVP and 300NO-PVP: the former exhibited a slightly better performance.

3.2 ESR and active-species-trapping experiments

Electron spin resonance spectroscopy (ESR) was performed to investigate the wavelength-dependent generation of photoactive species in the photocatalytic process. Several key conclusions can be drawn, based on the experimental results presented in Fig. 8. (1) A clearly decreased TEMPO-h⁺ signal, and strong DMPO-•O₂⁻ and DMPO-•OH signals in Fig.8a indicate that three main species of reactive free radicals,

h^+ , $\bullet O_2^-$ and $\bullet OH$, were produced using 300NO at 355 nm laser irradiation. In Fig.8b, the slightly decreased TEMPO- h^+ signal, and the distinct characteristic peaks of DMPO- $\bullet O_2^-$ verify that h^+ and $\bullet O_2^-$ were indeed generated using 300NO upon irradiation of 532 nm monochromatic light, while (at the same time) no DMPO- $\bullet OH$ was detected. (2) As shown in Fig.8c, all three main reactive species, h^+ , $\bullet O_2^-$ and $\bullet OH$, were detected separately for 300NO-PVP and 355 nm laser irradiation. The same reactive species were also detected, when the sample was irradiated with 532 nm monochromatic light - see Fig.8d. (3) Note that, for the same irradiation conditions, the signal of DMPO- $\bullet O_2^-$ with 300NO-PVP photocatalysis was much stronger than for the 300NO photocatalysis. This suggests that more active $\bullet O_2^-$ radicals were produced with 300NO-PVP. The same trend is also true for $\bullet OH$ radicals. For TEMPO- h^+ signals, the lower the intensity, the more h^+ were produced [38]. 300NO-PVP shows a weaker TEMPO- h^+ signal, which indicates a higher concentration of photogenerated holes than 300NO. (4) For both 300NO-PVP and 300NO, irradiation with 355 nm monochromatic light produced a much stronger DMPO- $\bullet O_2^-$ signal than irradiation with 532 nm. This suggests that more $\bullet O_2^-$ radicals were produced in the former. A similar trend is also observed for the h^+ and $\bullet OH$ radicals.

It is generally believed that wide bandgap semiconductors, such as TiO_2 ($E_g = 3.2$ eV) [39-41] and ZnO (3.1 – 3.4 eV) [42-44], can only absorb short-wavelength ultraviolet light, and they have only low utilization-capability for visible-light energy. In this experiment, both h^+ and $\bullet O_2^-$ radicals were directly detected, using Nb_2O_5 , upon irradiation with 532 nm monochromatic light. We found a 133 nm red shift with respect to its absorption edge (399 nm). This result can be explained using the previous valence-band analysis (see Fig. 4d), which showed that some localized states were lying above the valence-band edge of pure Nb_2O_5 (300NO). According to Shimakawa [12], an electron can be photoexcited from an isolated localized state to the conduction band and leaves behind a hole in the localized state. The resulting electrons can then react with O_2 to form $\bullet O_2^-$ radicals, while the photo-induced holes in the tail states cannot react with hydroxyl-ions (or H_2O) to form $\bullet OH$ radicals. This is probably because the positions of the localized states are more negative than the standard redox potentials of $\bullet OH/OH^-$ (+1.99 eV vs. NHE) and $\bullet OH/H_2O$ (+2.38 eV vs. NHE) [45, 46]. A more detailed discussion is presented in Section 3.4.

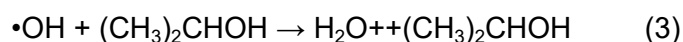
In a typical trapping experiment, BQ, EDTA-2Na, and IPA are most commonly used as scavengers to quench $\bullet O_2^-$, h^+ , and $\bullet OH$, respectively [47]. If the degradation activity is severely suppressed by (certain) scavengers, EDTA-2Na, for example, h^+ is

considered the pivotal reactive species in the degradation process. Otherwise, h^+ is not the major reactive species responsible for the photoreaction. In general, most conventional trapping experiments are performed under the assumption that the introduction of radical scavengers cannot affect the charge-transfer routes and the recombination rate of the photogenerated charge-carriers. On the other hand, many studies recently found a positive impact of the degradation rate occurred after the addition of certain scavengers - especially for hole scavengers such as AO [48-50] and ethanol [51], electron scavengers such as $AgNO_3$ [49, 52, 53], and $\bullet O_2^-$ scavengers such as BQ [53, 54]. This was found to be due to the decrease of the electron-hole recombination rate caused by the quenching effect of the scavengers. Hence, we propose a model that can describe the charge separation and transportation that occurs in a single-component photocatalyst in the radical-trapping experiments. It is based on the hypothesis that the electron-hole recombination rate depends on the addition of scavengers. This can help better interpret our experimental findings in the present study.

In Fig. 9a, the photogenerated holes can react directly with the adsorbed hydroxide ions (or water) to produce the $\bullet OH$ radicals [45, 46], as follows:



After IPA was added, it reacts with $\bullet OH$ radicals at a high rate to form inert intermediates (Reaction 3), which causes the termination of the radical chain reactions [55, 56]. Both Reactions, (1) and (2), can be sped-up due to the complete consumption of $\bullet OH$ radicals. More holes, however, are needed to react with OH^- or H_2O to form $\bullet OH$ radicals, and the recombination of photogenerated charge-carriers can be accordingly suppressed (to some degree) [56]. However, because the reported quantum yield for $\bullet OH$ production during the photocatalysis is much lower than for the hole generation [57], it can be concluded that the presence of IPA in the suspension has a limited effect on the recombination of photogenerated electron-hole pairs:

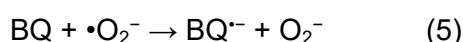


The effect of the presence of AO is displayed in Fig. 9b. AO would capture the photogenerated holes in the valence band during the photocatalysis reaction and leave the photogenerated electrons in the conduction band. As a result, the recombination of photogenerated carriers can be mitigated effectively. It is confirmed by many studies

that the photocatalytic reduction reaction can be significantly enhanced by the addition of AO as hole scavenger [58-60]. Accordingly, more photogenerated electrons become available to produce $\cdot\text{O}_2^-$ radicals for photocatalytic reactions, according to the equation:



BQ is very reactive toward $\cdot\text{O}_2^-$ due to its ability to trap this anion radical via a simple electron-transfer mechanism, (5) [61]:



The consumption of $\cdot\text{O}_2^-$ in the presence of BQ can promote the reaction rate of e^- and O_2 and cause more electrons to be trapped. Most of these electrons could instantly recombine with the photogenerated holes if there is no BQ. In this way, the addition of BQ can help prolong the lifetime of the photogenerated holes, which can directly participate in the photocatalytic reactions – see Fig. 9c.

In order to identify the active species of samples 300NO and 300NO-PVP, which are involved in the photodegradation of MB for different light-sources, a sequence of trapping experiments was carried out:

(1) Quenching $\cdot\text{OH}$ radicals using IPA or TBA

To evaluate the role of $\cdot\text{OH}$ radicals in the photocatalytic process, both IPA (0.1 mM) and TBA (0.1 mM) were used as scavengers. As shown in Fig. 10, independent of wavelength, the degradation efficiency of MB using the samples 300NO and 300NO-PVP was almost not affected when IPA or TBA was added. Although the ESR spectrum in Fig.8a shows clear evidence of the production of $\cdot\text{OH}$ radicals for 300NO and 355 nm laser irradiation, the addition of IPA or TBA neither decreased nor increased (clearly) the removal efficiency of MB upon irradiation with 365 nm LED light. A similar result was observed for 300NO-PVP: The $\cdot\text{OH}$ scavengers showed only a minor effect on the degradation rate of MB for the different wavelengths. However, the ESR spectra in Figs.8c and 8d show strong $\cdot\text{OH}$ signals for 300NO upon irradiation with 355 and 532 nm light. The results indicate that the $\cdot\text{OH}$ radicals, which were produced by both 300NO and 300NO-PVP, played a very limited role in the decomposition of MB at any wavelength.

(2) Quenching $\cdot\text{O}_2^-$ radicals via BQ

0.1 mM BQ was added to the suspension to act as scavenger of $\cdot\text{O}_2^-$ radicals and to study its potential impact on the photocatalytic reaction. As shown in Fig. 10a(i) and 10a(ii), upon irradiation with 365 and 420 nm LED light, the photocatalytic degradation

of MB for 300NO was significantly boosted by adding BQ, and 100 % MB was removed in 20 min. As shown in Fig. 10a(iii), the enhancement of the photocatalytic degradation of MB (by adding BQ) weakened after irradiation with 535 nm LED light. In Fig. 10a(iv), BQ shows no apparent effects on the photocatalytic degradation reaction upon irradiation with 630 nm LED light. As shown in Fig. 10b(i), under 365 nm LED light irradiation, the photocatalytic degradation of MB over 300NO-PVP was enhanced after adding BQ, and 100 % MB was removed within 40 min. For 420 nm LED light irradiation (Fig. 10b(ii)), the removal efficiency was further enhanced, and all MB molecules were completely removed in 20 min. As shown in Figs. 10b(iii), only 92% MB was removed in 80 min after irradiation with 535 nm LED light. Under 630 nm irradiation, the removal efficiency was only slightly improved compared to the control - see Fig. 10b(iv). Figs. 10a(v) and 10b(v) show the trapping experiments performed with white-light for the samples 300NO and 300NO-PVP, respectively. When trapping $\cdot\text{O}_2^-$, for both 300NO and 300NO-PVP, the addition of BQ greatly improved the removal efficiency of MB.

(3) Quenching holes using AO or EDTA-2Na

The effect of EDTA-2Na and AO as hole scavengers in the photocatalytic activity of samples 300NO and 300NO-PVP was studied. For both 300NO and 300NO-PVP, in most cases, the addition of AO resulted in a higher reaction rate than for EDTA-2Na. This suggests that AO is a stronger hole-scavenger and has a better ability to trap holes. For sample 300NO, the enhancement in the photocatalytic reaction (by adding AO) is not clear when 365 nm, 630 nm, and white LEDs were used as light sources. However, the removal efficiency was notably improved compared to the control upon irradiation with 420 and 535 nm LED lights. Both the high adsorption capacity as well as the high photodegradation rate of 300NO likely affected the active species trapping experiments. For 300NO-PVP, the enhancement effect on the MB removal (by adding AO) was almost equivalent to using four monochromatic LEDs as well as the white LED as light sources. About 92% MB was successfully removed within the first 20 min.

(4) Wavelength dependency of holes and superoxide radicals ($\cdot\text{O}_2^-$)

Based on these findings and the discussed results shown in Fig. 9, the boosted removal efficiency (by adding AO) can be ascribed to the production of excess $\cdot\text{O}_2^-$, which is due to trapping of holes. On the other hand, the enhanced photoactivity in the presence of BQ can be attributed to the improved survival rate of photogenerated holes.

The photogenerated holes for 300NO were very active at 365 and 420 nm. At 535 nm, the role of the photogenerated holes became less important. At 630 nm, perhaps the photogenerated holes were inactive for MB. In 300NO-PVP, it is more clearly seen

that the photogenerated holes are crucial in the 365-420 nm range. Subsequently, they become less important with increasing wavelength.

For 300NO, although the trapping experiment was affected by the high adsorption capacity and high photodegradation rate of the material, $\bullet\text{O}_2^-$ were certainly produced at 365 nm (according to the ESR results) at 355 nm. In addition, $\bullet\text{O}_2^-$ was apparently active during the photodegradation of MB at 420 and 535 nm and probably plays a (negligible) role at 630 nm according to the results of the trapping experiments. For 300NO-PVP, $\bullet\text{O}_2^-$ showed little wavelength dependence and it was consistently active at wavelengths ranging from 365 to 630 nm.

3.3 Photostability and reusability evaluation

To check the stability and efficiency of the photocatalytic performance of the 300NO and 300NO-PVP, repeated runs of photocatalytic degradation experiments of MB, under white light, are carried out - see Fig.11. AO and BQ were also added to further examine their roles in the enhancement of the photocatalytic degradation. During the first cycle, the removal efficiency of MB with 300NO and 300NO-PVP, without adding AO or BQ, were both nearly 100%. In the second cycle, the removal rate of MB dye for 300NO significantly decreased to 66.01%. It was increased to 93.30% and 71.53%, however, in the presence of 0.1 mM BQ and 0.1 mM AO, respectively. In addition, the degradation percentages for 300NO-PVP significantly increased (from 65.12% to 90.95% and 78.01%) with the addition of 0.1 mM BQ and 0.1 mM AO, respectively. It is generally believed that the high adsorption capacity of the photocatalyst can positively affect its photodegradation by providing more accessible reactive sites. However, some researchers argued that excessive adsorption of dye molecules on the surface of catalysts might reduce the formation rate of reactive species and hinder the penetration of incident light, which can make the photodegradation worse [62-64]. Our findings agree with this viewpoint in the sense that the long-term cyclability in photocatalytic application can become worse after excessive adsorption of pollutant molecules on the surface of the photocatalysts.

3.4 Photocatalytic mechanism

To understand the photocatalytic mechanism, the electronic structures of 300NO and 300NO-PVP were analyzed. According to the UV-Vis absorbance spectra of 300NO and 300NO-PVP (Fig. 5b), we calculated their bandgaps (E_g) to be 3.32 and 2.99 eV, respectively. The potentials of the valence bands, E_{VB} , were obtained as 2.86 eV and 2.60 eV vs. NHE for 300NO and 300NO-PVP, respectively - see Fig. 4d.

Therefore, the CB positions of 300NO and 300NO-PVP were determined, respectively, -0.47 and -0.39 eV vs NHE. This was done using the empirical formula: $E_{CB} = E_{VB} - E_g$.

For sample 300NO, the production of $\bullet\text{O}_2^-$ radicals and h^+ , at wavelengths greater than the absorption edge (399 nm), can be explained by the presence of localized states in the forbidden gap - see Fig.12a. These localized states can be produced by disorder, which can be created by e.g., oxygen vacancies and oxygen interstitials [12, 65-68]. Oxygen vacancies create some new discrete energy levels near the conduction band, while oxygen interstitials introduce localized states near the valence band [12, 65-69]. Upon irradiation with 365 nm monochromatic light, an electron can be excited from the valence band to the conduction band, leaving a hole in the valence band. Upon irradiation with 420, 535, and 630 nm monochromatic light (because the photon energies are much lower than the bandgap energy of 300NO), the presence of localized states provides two different channels for light harvesting: (1) excitation of electrons from the localized states near the valence band to the conduction band; (2) excitation of electrons from the localized states above the valence band to the localized states below the conduction band. The lower the photon energy, the lower is the probability for electrons transfer to the conduction band. If the potential for electrons in the localized states is more negative than $E(\text{O}_2 / \bullet\text{O}_2^-)$ (-0.33 eV vs NHE) [45, 46], they can react with O_2 to form $\bullet\text{O}_2^-$ radicals. If the position of the localized states above valence band is more positive than the standard redox potentials of $\bullet\text{OH}/\text{OH}^-$ (+1.99 eV vs. NHE) and $\bullet\text{OH}/\text{H}_2\text{O}$ (+2.38 eV vs. NHE) [45, 46], the resulting holes can react with hydroxyl ions or H_2O and form $\bullet\text{OH}$ radicals.

As for sample 300NO-PVP, carbon doping can significantly affect the electronic structure of the material [11, 32, 70-75]. Moreover, bandgap-narrowing can be induced, which may account for the red shift of the absorption edge toward the visible, and more localized occupied states can be introduced within the forbidden gap. As shown in Fig.12b, an electron can be excited from the valence band to the conduction band, and a hole is left behind in the valence band under the irradiation of 365 nm monochromatic light. Upon irradiation with 420, 535, and 630 nm monochromatic light, the photon energies were not high enough to excite electrons from the valence to the conduction band. The light harvesting behavior of 300NO-PVP is very similar to that of 300NO: (1) excitation of electrons from the localized states above valence band to conduction band; (2) excitation of electrons from the localized states above valence band to the localized states below the conduction band. Due to bandgap narrowing as well as the presence of more localized occupied states within the gap, the photogenerated

electrons (or holes) are more likely to take part in redox reactions to produce $\cdot\text{O}_2^-$ or $\cdot\text{OH}$ radicals compared to 300NO. For example, the photon energy associated with 535 nm (2.32 eV) is large enough to excite electrons in 300NO-PVP from a localized state slightly lower than $E(\cdot\text{OH}/\text{OH}^-)$ (+1.99 eV vs. NHE) to a localized level that is close to the standard redox potentials of $E(\text{O}_2/\cdot\text{O}_2^-)$ (-0.33 eV vs NHE). Both $\cdot\text{O}_2^-$ and $\cdot\text{OH}$ can likely be created using 300NO-PVP under these conditions, while, at the same time, only $\cdot\text{O}_2^-$ can be produced using 300NO.

Furthermore, the role of holes in the photocatalytic reaction declined with increasing wavelength, while $\cdot\text{O}_2^-$ showed little wavelength dependency, especially for C-doped Nb_2O_5 . This is probably because the localized states near the valence band were more diffuse than those near the conduction band, which means that the oxidative potential of photogenerated holes was more susceptible to photon energy. Most importantly, most of the localized states near the conduction band are likely more negative than the standard redox potentials of $E(\text{O}_2/\cdot\text{O}_2^-)$ (-0.33 eV vs NHE). As a result, the photogenerated electrons in the localized states have a high probability to react with O_2 and produce $\cdot\text{O}_2^-$ radicals.

4. Conclusions

In this contribution, both pure and carbon-doped Nb_2O_5 were prepared using a facile calcination-assisted hydrothermal method. Both were chosen as model photocatalysts to detect the production of reactive species as a function of excitation wavelength. The main results can be summarized as follows:

- (1) Carbon doping can not only shift the top of the valence band of Nb_2O_5 upwards (for band-gap narrowing) but also increase both the separation and transfer efficiency of photogenerated charge-carriers.
- (2) Due to localized states, the absorption of photons can also occur for photon energies that are lower than the bandgap, which can lead to the wavelength-dependent generation of reactive species in the photocatalytic process. All three main active species, $\cdot\text{OH}$ radicals, holes and $\cdot\text{O}_2^-$ radicals, could be created at 355 nm for both pure and C-doped Nb_2O_5 . Only h^+ and $\cdot\text{O}_2^-$ radicals were produced, however, using pure Nb_2O_5 at 532 nm (which is well beyond its absorption edge of 399 nm), while, at the same time, all the three reactive species can be produced using C-doped Nb_2O_5 .
- (3) $\cdot\text{O}_2^-$ and h^+ were suggested to be the main active species among the decomposing MB molecules, while $\cdot\text{OH}$ appears of minimal significance. The photogenerated holes were crucial for the range of 365–420 nm. Nevertheless,

they became less active with increasing wavelength. $\bullet\text{O}_2^-$ showed little wavelength dependence, and they were consistently active from 365 to 630 nm, especially for C-doped Nb_2O_5 .

Declaration of Competing Interest

The authors declare that they have no known competing financial interests or personal relationships that could have appeared to influence the work reported in this paper.

Acknowledgements

This work was supported by the postdoctoral fellowships from the China Scholarship Council (Grant No. 201708505127), the Science and Technology Research Program of Chongqing Municipal Education Commission (Grant No. KJQN201801419 and Grant No. KJQN202001440) and the Natural Science Foundation of Chongqing (Grant No. cstc2018jcyjAX0189).

References

- [1] Y.J. Lai, D.J.J. Lee, Pollutant degradation with mediator Z-scheme heterojunction photocatalyst in water: A review, *Chemosphere* (2021) 131059. <https://doi.org/https://doi.org/10.1016/j.chemosphere.2021.131059>.
- [2] S. Meng, J. Zhang, S. Chen, S. Zhang, W.J. Huang, Perspective on construction of heterojunction photocatalysts and the complete utilization of photogenerated charge carriers, *Applied Surface Science* 476 (2019) 982-992. <https://doi.org/https://doi.org/10.1016/j.apsusc.2019.01.246>.
- [3] B. Chen, L. Zhou, Y. Tian, J. Yu, J. Lei, L. Wang, Y. Liu, J.J. Zhang, Z-scheme inverse opal CN/BiOBr photocatalysts for highly efficient degradation of antibiotics, *Physical Chemistry Chemical Physics* 21(24) (2019) 12818-12825. <https://doi.org/10.1039/C9CP01495K>.
- [4] L.-W. Zhang, H.-B. Fu, Y.-F. Zhu, Efficient TiO₂ Photocatalysts from Surface Hybridization of TiO₂ Particles with Graphite-like Carbon, *Advanced Functional Materials* 18(15) (2008) 2180-2189. <https://doi.org/10.1002/adfm.200701478>.
- [5] S.C. Yan, Z.S. Li, Z.G. Zou, Photodegradation performance of g-C₃N₄ fabricated by directly heating melamine, *Langmuir* 25(17) (2009) 10397-401. <https://doi.org/10.1021/la900923z>.
- [6] S. Wu, J. Sun, Q. Li, Z.D. Hood, S. Yang, T. Su, R. Peng, Z. Wu, W. Sun, P.R.J.A.a.m. Kent, Effects of surface terminations of 2D Bi₂WO₆ on photocatalytic hydrogen evolution from water splitting, *ACS applied materials & interfaces* 12(17) (2020) 20067-20074. <https://doi.org/https://doi-org.mtroyal.80599.net/10.1021/acsami.0c01802>.
- [7] S. Sun, G. Shen, Z. Chen, L. Pan, X. Zhang, J.-J. Zou, Harvesting urbach tail energy of ultrathin amorphous nickel oxide for solar-driven overall water splitting up to 680 nm, *Applied Catalysis B: Environmental* 285 (2021). <https://doi.org/10.1016/j.apcatb.2020.119798>.
- [8] L. Ran, J. Hou, S. Cao, Z. Li, Y. Zhang, Y. Wu, B. Zhang, P. Zhai, L.J. Sun, Defect engineering of photocatalysts for solar energy conversion, *Solar RRL* 4(4) (2020) 1900487. <https://doi.org/> <https://doi-org.ucl.80599.net/10.1002/solr.201900487>.
- [9] Z. Wang, Y. Liu, B. Huang, Y. Dai, Z. Lou, G. Wang, X. Zhang, X. Qin, Progress on extending the light absorption spectra of photocatalysts, *Phys Chem Chem Phys* 16(7) (2014) 2758-74. <https://doi.org/10.1039/c3cp53817f>.
- [10] S.B. Patil, P.S. Basavarajappa, N. Ganganagappa, M.S. Jyothi, A.V. Raghu, K.R. Reddy, Recent advances in non-metals-doped TiO₂ nanostructured photocatalysts for visible-light driven hydrogen production, CO₂ reduction and air purification, *International Journal of Hydrogen Energy* 44(26) (2019) 13022-13039. <https://doi.org/10.1016/j.ijhydene.2019.03.164>.
- [11] X. Chen, C.J. Burda, The electronic origin of the visible-light absorption properties of C-, N-and S-doped TiO₂ nanomaterials, *Journal of the American Chemical Society* 130(15) (2008) 5018-5019. <https://doi.org/https://doi-org.mtroyal.80599.net/10.1021/ja711023z>.
- [12] K. Shimakawa, J. Singh, S.J. O'Leary, *Optical Properties of Materials and Their Applications*, Second Edition, (2019) 67-81. <https://doi.org/https://doi->

[org.ucl.80599.net/10.1002/9781119506003.ch3](https://doi.org/10.1002/9781119506003.ch3).

[13] Z. Lin, C. Du, B. Yan, G. Yang, Two-dimensional amorphous CoO photocatalyst for efficient overall water splitting with high stability, *Journal of Catalysis* 372 (2019) 299-310. <https://doi.org/10.1016/j.jcat.2019.03.025>.

[14] A. Zanatta, I.J. Chambouleyron, Absorption edge, band tails, and disorder of amorphous semiconductors, *Physical Review B* 53(7) (1996) 3833. <https://doi.org/https://doi.org.yorku.80599.net/10.1103/PhysRevB.53.3833>.

[15] L. Tian, W. Xie, X. Wu, B. Guo, G. Xie, P. Cheng, X. Liu, J.R.J. Gong, Overall Regulation of Exciton Dynamics by Defect Engineering in Polymeric Photocatalysts for Hydrogen Evolution, *The Journal of Physical Chemistry C* 124(45) (2020) 24667-24676. <https://doi.org/https://doi.org.mtroyal.80599.net/10.1021/acs.jpcc.0c08830>.

[16] H. Tong, S. Ouyang, Y. Bi, N. Umezawa, M. Oshikiri, J.J. Ye, Nano - photocatalytic materials: possibilities and challenges, *Advanced materials* 24(2) (2012) 229-251. <https://doi.org/https://doi.org.ucl.80599.net/10.1002/adma.201102752>.

[17] W. Wang, W. Zhao, H. Zhang, X. Dou, H.J. Shi, 2D/2D step-scheme α -Fe₂O₃/Bi₂WO₆ photocatalyst with efficient charge transfer for enhanced photo-Fenton catalytic activity, *Chinese Journal of Catalysis* 42(1) (2021) 97-106. [https://doi.org/https://doi.org/10.1016/S1872-2067\(20\)63602-6](https://doi.org/https://doi.org/10.1016/S1872-2067(20)63602-6).

[18] M. Mousavi, A. Habibi-Yangjeh, D.J.J.o.m.s. Seifzadeh, technology, Novel ternary g-C₃N₄/Fe₃O₄/MnWO₄ nanocomposites: synthesis, characterization, and visible-light photocatalytic performance for environmental purposes, *Journal of materials science* 34(9) (2018) 1638-1651. <https://doi.org/https://doi.org/10.1016/j.jmst.2018.05.004>.

[19] C. Yang, J. Yang, X. Duan, G. Hu, Q. Liu, S. Ren, J. Li, M.J. Kong, Roles of photo-generated holes and oxygen vacancies in enhancing photocatalytic performance over CeO₂ prepared by molten salt method, *Advanced Powder Technology* 31(9) (2020) 4072-4081. <https://doi.org/https://doi.org/10.1016/j.apt.2020.08.017>.

[20] T. Jiang, K. Wang, T. Guo, X. Wu, G.J. Zhang, Fabrication of Z-scheme MoO₃/Bi₂O₄ heterojunction photocatalyst with enhanced photocatalytic performance under visible light irradiation, *Chinese Journal of Catalysis* 41(1) (2020) 161-169. [https://doi.org/https://doi.org/10.1016/S1872-2067\(19\)63391-7](https://doi.org/https://doi.org/10.1016/S1872-2067(19)63391-7).

[21] L. Lu, G. Wang, M. Zou, J. Wang, J.J. Li, Effects of calcining temperature on formation of hierarchical TiO₂/g-C₃N₄ hybrids as an effective Z-scheme heterojunction photocatalyst, *Applied Surface Science* 441 (2018) 1012-1023. <https://doi.org/https://doi.org/10.1016/j.apsusc.2018.02.080>.

[22] D. Chandra, A.J. Bhaumik, Photoluminescence behavior of new mesoporous titanium-composites synthesized by using bidentate structure directing agents, *Microporous mesoporous materials* 101(3) (2007) 348-354. <https://doi.org/https://doi.org/10.1016/j.micromeso.2006.11.027>.

[23] C. Peng, X. Xie, W. Xu, T. Zhou, P. Wei, J. Jia, K. Zhang, Y. Cao, H. Wang, F.J.C.E.J. Peng, Engineering highly active Ag/Nb₂O₅@Nb₂CTx (MXene) photocatalysts via steering charge kinetics strategy, *Chemical Engineering Journal* 421 (2021) 128766.

[24] K. Su, Y. Wang, C. Zhang, Z. Gao, J. Han, F.J. Wang, Tuning the Pt species on Nb₂O₅ by support-induced modification in the photocatalytic transfer hydrogenation of phenylacetylene, *Applied Catalysis B: Environmental* 298 (2021) 120554.

<https://doi.org/https://doi.org/10.1016/j.apcatb.2021.120554>.

[25] D. Zu, H. Song, Y. Wang, Z. Chao, Z. Li, G. Wang, Y. Shen, C. Li, J.J.A.C.B.E. Ma, One-pot in-situ hydrothermal synthesis of CdS/Nb₂O₅/Nb₂C heterojunction for enhanced visible-light-driven photodegradation, *Applied Catalysis B: Environmental*

277 (2020) 119140. <https://doi.org/https://doi.org/10.1016/j.apcatb.2020.119140>.

[26] C. Cui, R. Guo, E. Ren, H. Xiao, X. Lai, Q. Qin, S. Jiang, H. Shen, M. Zhou, W. Qin, Facile hydrothermal synthesis of rod-like Nb₂O₅/Nb₂CTx composites for visible-light driven photocatalytic degradation of organic pollutants, *Environ Res* 193 (2021) 110587.

<https://doi.org/10.1016/j.envres.2020.110587>.

[27] T. Su, R. Peng, Z.D. Hood, M. Naguib, I.N. Ivanov, J.K. Keum, Z. Qin, Z. Guo, Z. Wu, One - Step Synthesis of Nb₂O₅/C/Nb₂C (MXene) Composites and Their Use as Photocatalysts for Hydrogen Evolution, *ChemSusChem* 11(4) (2018) 688-699.

<https://doi.org/10.1002/cssc.201702317>.

[28] M.T. Marques, A.M. Ferraria, J.B. Correia, A.M.B.d. Rego, R. Vilar, XRD, XPS and SEM characterisation of Cu–NbC nanocomposite produced by mechanical alloying, *Materials Chemistry and Physics* 109(1) (2008) 174-180.

<https://doi.org/10.1016/j.matchemphys.2007.10.032>.

[29] P. Jing, K. Liu, L. Soule, J. Wang, T. Li, B. Zhao, M. Liu, Engineering the architecture and oxygen deficiency of T-Nb₂O₅-carbon-graphene composite for high-rate lithium-ion batteries, *Nano Energy* 89 (2021). <https://doi.org/10.1016/j.nanoen.2021.106398>.

[30] S. Wang, X. Zhang, S. Li, Y. Fang, L. Pan, J.J. Zou, C-doped ZnO ball-in-ball hollow microspheres for efficient photocatalytic and photoelectrochemical applications, *J Hazard Mater* 331 (2017) 235-245. <https://doi.org/10.1016/j.jhazmat.2017.02.049>.

[31] L. Pan, T. Muhammad, L. Ma, Z.-F. Huang, S. Wang, L. Wang, J.-J. Zou, X. Zhang, MOF-derived C-doped ZnO prepared via a two-step calcination for efficient photocatalysis, *Applied Catalysis B: Environmental* 189 (2016) 181-191. <https://doi.org/10.1016/j.apcatb.2016.02.066>.

[32] Y.T. Lin, C.H. Weng, Y.H. Lin, C.C. Shiesh, F.Y. Chen, Effect of C content and calcination temperature on the photocatalytic activity of C-doped TiO₂ catalyst, *Separation and Purification Technology* 116 (2013) 114-123. <https://doi.org/10.1016/j.seppur.2013.05.018>.

[33] J. Yu, G. Dai, Q. Xiang, M. Jaroniec, Fabrication and enhanced visible-light photocatalytic activity of carbon self-doped TiO₂ sheets with exposed {001} facets, *J. Mater. Chem.* 21(4) (2011) 1049-1057. <https://doi.org/10.1039/c0jm02217a>.

[34] Q. Han, C. Wu, H. Jiao, R. Xu, Y. Wang, J. Xie, Q. Guo, J. Tang, Rational Design of High-Concentration Ti(3+) in Porous Carbon-Doped TiO₂ Nanosheets for Efficient Photocatalytic Ammonia Synthesis, *Adv Mater* 33(9) (2021) e2008180.

<https://doi.org/10.1002/adma.202008180>.

[35] V. Nadtochenko, N. Denisov, A. Gorenberg, Y. Kozlov, P. Chubukov, J.A. Rengifo, C. Pulgarin, J. Kiwi, Correlations for photocatalytic activity and spectral features of the absorption band edge of TiO₂ modified by thiourea, *Applied Catalysis B: Environmental* 91(1-2) (2009) 460-469. <https://doi.org/10.1016/j.apcatb.2009.06.015>.

[36] T. Xiong, H. Huang, Y. Sun, F. Dong, In situ synthesis of a C-doped (BiO)₂CO₃ hierarchical self-assembly effectively promoting visible light photocatalysis, *Journal of Materials Chemistry A* 3(11) (2015) 6118-6127. <https://doi.org/10.1039/c5ta00103j>.

[37] J. Wu, X. Chen, C. Li, Y. Qi, X. Qi, J. Ren, B. Yuan, B. Ni, R. Zhou, J. Zhang, T. Huang,

Hydrothermal synthesis of carbon spheres – BiOI/BiOIO₃ heterojunctions for photocatalytic removal of gaseous Hg⁰ under visible light, *Chemical Engineering Journal* 304 (2016) 533-543. <https://doi.org/10.1016/j.cej.2016.06.128>.

[38] X. Yang, L. Tian, X. Zhao, H. Tang, Q. Liu, G. Li, Interfacial optimization of g-C₃N₄-based Z-scheme heterojunction toward synergistic enhancement of solar-driven photocatalytic oxygen evolution, *Applied Catalysis B: Environmental* 244 (2019) 240-249. <https://doi.org/10.1016/j.apcatb.2018.11.056>.

[39] X. Yang, C. Cao, K. Hohn, L. Erickson, R. Maghirang, D. Hamal, K. Klabunde, Highly visible-light active C- and V-doped TiO₂ for degradation of acetaldehyde, *Journal of Catalysis* 252(2) (2007) 296-302. <https://doi.org/10.1016/j.jcat.2007.09.014>.

[40] Y. Wang, C. Yang, A. Chen, W. Pu, J. Gong, Influence of yolk-shell Au@TiO₂ structure induced photocatalytic activity towards gaseous pollutant degradation under visible light, *Applied Catalysis B: Environmental* 251 (2019) 57-65. <https://doi.org/10.1016/j.apcatb.2019.03.056>.

[41] S. Wu, H. Hu, Y. Lin, J. Zhang, Y.H. Hu, Visible light photocatalytic degradation of tetracycline over TiO₂, *Chemical Engineering Journal* 382 (2020). <https://doi.org/10.1016/j.cej.2019.122842>.

[42] D.T.C. Nguyen, H.T.N. Le, T.T. Nguyen, T.T.T. Nguyen, L.G. Bach, T.D. Nguyen, T.V. Tran, Multifunctional ZnO nanoparticles bio-fabricated from *Canna indica* L. flowers for seed germination, adsorption, and photocatalytic degradation of organic dyes, *J Hazard Mater* 420 (2021) 126586. <https://doi.org/10.1016/j.jhazmat.2021.126586>.

[43] C. Rodwihok, K. Charoensri, D. Wongratanaphisan, W.M. Choi, S.H. Hur, H.J. Park, J.S. Chung, Improved photocatalytic activity of surface charge functionalized ZnO nanoparticles using aniline, *Journal of Materials Science & Technology* 76 (2021) 1-10. <https://doi.org/10.1016/j.jmst.2020.09.041>.

[44] Z. Chen, Y. Fang, L. Wang, X. Chen, W. Lin, X. Wang, Remarkable oxygen evolution by Co-doped ZnO nanorods and visible light, *Applied Catalysis B: Environmental* 296 (2021). <https://doi.org/10.1016/j.apcatb.2021.120369>.

[45] L. Xie, T. Du, J. Wang, Y. Ma, Y. Ni, Z. Liu, L. Zhang, C. Yang, J. Wang, Recent advances on heterojunction-based photocatalysts for the degradation of persistent organic pollutants, *Chemical Engineering Journal* 426 (2021). <https://doi.org/10.1016/j.cej.2021.130617>.

[46] Y. Yuan, R.T. Guo, L.F. Hong, X.Y. Ji, Z.D. Lin, Z.S. Li, W.G. Pan, A review of metal oxide-based Z-scheme heterojunction photocatalysts: actualities and developments, *Materials Today Energy* 21 (2021). <https://doi.org/10.1016/j.mtener.2021.100829>.

[47] M. Ranjeh, F. Beshkar, M. Salavati-Niasari, Sol-gel synthesis of novel Li-based boron oxides nanocomposite for photodegradation of azo-dye pollutant under UV light irradiation, *Composites Part B: Engineering* 172 (2019) 33-40. <https://doi.org/10.1016/j.compositesb.2019.05.085>.

[48] Z. Song, Y. He, Novel AgCl/Ag/AgFeO₂ Z-scheme heterostructure photocatalyst with enhanced photocatalytic and stability under visible light, *Applied Surface Science* 420 (2017) 911-918. <https://doi.org/10.1016/j.apsusc.2017.05.212>.

[49] F. Mushtaq, X. Chen, H. Torlakcik, B.J. Nelson, S. Pané, Enhanced catalytic degradation of organic pollutants by multi-stimuli activated multiferroic nanoarchitectures, *Nano Research* 13(8) (2020) 2183-2191. <https://doi.org/10.1007/s12274-020-2829-2>.

- [50] A.D. Xie, M.G. Hu, Y.H. Luo, X.G. Zhu, Z.H. Wang, W.Y. Geng, H. Zhang, D.E. Zhang, H. Zhang, Synthesis of a stable iron(III)–organic framework for a visible light induced simultaneous photocatalytic reduction of Cr(VI) and the degradation of organic dyes in water, *New Journal of Chemistry* 45(30) (2021) 13406-13414. <https://doi.org/10.1039/d1nj01643a>.
- [51] H. Wang, X. Yuan, Y. Wu, G. Zeng, X. Chen, L. Leng, Z. Wu, L. Jiang, H. Li, Facile synthesis of amino-functionalized titanium metal-organic frameworks and their superior visible-light photocatalytic activity for Cr(VI) reduction, *J Hazard Mater* 286 (2015) 187-94. <https://doi.org/10.1016/j.jhazmat.2014.11.039>.
- [52] W. Li, D. Li, J. Wang, Y. Shao, J. You, F. Teng, Exploration of the active species in the photocatalytic degradation of methyl orange under UV light irradiation, *Journal of Molecular Catalysis A: Chemical* 380 (2013) 10-17. <https://doi.org/10.1016/j.molcata.2013.09.001>.
- [53] L. Sun, B. Li, X. Chu, N. Sun, Y. Qu, X. Zhang, I. Khan, L. Bai, L. Jing, Synthesis of Si–O-Bridged g-C₃N₄/WO₃ 2D-Heterojunctional Nanocomposites as Efficient Photocatalysts for Aerobic Alcohol Oxidation and Mechanism Insight, *ACS Sustainable Chemistry & Engineering* 7(11) (2019) 9916-9927. <https://doi.org/10.1021/acssuschemeng.9b00711>.
- [54] D. Lin, M. Gao, L. You, Y. Li, Z. Li, L. Guo, T. Li, M. Liu, Fabrication of novel Ag/AgVO₃/WO₃ homojunction/heterojunction nanomaterials with highly enhanced photocatalytic activity- Investigation on type I plus Z-scheme mechanism, *Journal of Alloys and Compounds* 846 (2020). <https://doi.org/10.1016/j.jallcom.2020.156274>.
- [55] G.V. Buxton, C.L. Greenstock, W.P. Helman, A.B. Ross, Critical Review of rate constants for reactions of hydrated electrons, hydrogen atoms and hydroxyl radicals ($\cdot\text{OH}/\cdot\text{O}^-$ in Aqueous Solution, *Journal of Physical and Chemical Reference Data* 17(2) (1988) 513-886. <https://doi.org/10.1063/1.555805>.
- [56] J. Jose, S. Ramanujam, L. Philip, Applicability of pulsed corona discharge treatment for the degradation of chloroform, *Chemical Engineering Journal* 360 (2019) 1341-1354. <https://doi.org/10.1016/j.cej.2018.10.199>.
- [57] K.-i. Ishibashi, A. Fujishima, T. Watanabe, K.J.J.o.p. Hashimoto, Quantum yields of active oxidative species formed on TiO₂ photocatalyst, *Journal of photochemistry photobiology A: chemistry* 134(1-2) (2000) 139-142. [https://doi.org/https://doi.org/10.1016/S1010-6030\(00\)00264-1](https://doi.org/https://doi.org/10.1016/S1010-6030(00)00264-1).
- [58] R. Yuan, C. Yue, J. Qiu, F. Liu, A.J. Li, Highly efficient sunlight-driven reduction of Cr (VI) by TiO₂@NH₂-MIL-88B (Fe) heterostructures under neutral conditions, *Applied Catalysis B: Environmental* 251 (2019) 229-239.
- [59] W. Wu, S. Liang, Y. Chen, L. Shen, H. Zheng, L. Wu, High efficient photocatalytic reduction of 4-nitroaniline to p-phenylenediamine over microcrystalline SrBi₂Nb₂O₉, *Catalysis Communications* 17 (2012) 39-42. <https://doi.org/10.1016/j.catcom.2011.10.012>.
- [60] Y.-H. Chang, M.-C. Wu, Enhanced Photocatalytic Reduction of Cr(VI) by Combined Magnetic TiO₂-Based NFs and Ammonium Oxalate Hole Scavengers, *Catalysts* 9(1) (2019). <https://doi.org/10.3390/catal9010072>.
- [61] P. Raja, A. Bozzi, H. Mansilla, J. Kiwi, Evidence for superoxide-radical anion, singlet oxygen and OH-radical intervention during the degradation of the lignin model compound (3-methoxy-4-hydroxyphenylmethylcarbinol), *Journal of Photochemistry and Photobiology A: Chemistry* 169(3) (2005) 271-278. <https://doi.org/10.1016/j.jphotochem.2004.07.009>.
- [62] S. Liu, M. Li, S. Li, H. Li, L. Yan, Synthesis and adsorption/photocatalysis performance of

pyrite FeS₂, *Applied Surface Science* 268 (2013) 213-217. <https://doi.org/10.1016/j.apsusc.2012.12.061>.

[63] L.J. Xu, W. Chu, L. Gan, Environmental application of graphene-based CoFe₂O₄ as an activator of peroxymonosulfate for the degradation of a plasticizer, *Chemical Engineering Journal* 263 (2015) 435-443. <https://doi.org/10.1016/j.cej.2014.11.065>.

[64] S. Deepracha, A. Ayril, M. Ogawa, Acceleration of the photocatalytic degradation of organics by in-situ removal of the products of degradation, *Applied Catalysis B: Environmental* 284 (2021). <https://doi.org/10.1016/j.apcatb.2020.119705>.

[65] S. Kuriakose, B. Satpati, S. Mohapatra, Enhanced photocatalytic activity of Co doped ZnO nanodisks and nanorods prepared by a facile wet chemical method, *Phys Chem Chem Phys* 16(25) (2014) 12741-9. <https://doi.org/10.1039/c4cp01315h>.

[66] S.K. Cushing, F. Meng, J. Zhang, B. Ding, C.K. Chen, C.-J. Chen, R.-S. Liu, A.D. Bristow, J. Bright, P. Zheng, N. Wu, Effects of Defects on Photocatalytic Activity of Hydrogen-Treated Titanium Oxide Nanobelts, *ACS Catalysis* 7(3) (2017) 1742-1748. <https://doi.org/10.1021/acscatal.6b02177>.

[67] S. Bai, N. Zhang, C. Gao, Y. Xiong, Defect engineering in photocatalytic materials, *Nano Energy* 53 (2018) 296-336. <https://doi.org/10.1016/j.nanoen.2018.08.058>.

[68] A. Naldoni, M. Allieta, S. Santangelo, M. Marelli, F. Fabbri, S. Cappelli, C.L. Bianchi, R. Psaro, V. Dal Santo, Effect of nature and location of defects on bandgap narrowing in black TiO₂ nanoparticles, *J Am Chem Soc* 134(18) (2012) 7600-3. <https://doi.org/10.1021/ja3012676>.

[69] F.J. Knorr, C.C. Mercado, J.L.J. McHale, Trap-state distributions and carrier transport in pure and mixed-phase TiO₂: influence of contacting solvent and interphasial electron transfer, *The Journal of Physical Chemistry C* 112(33) (2008) 12786-12794. <https://doi.org/https://doi.org.mtroyal.80599.net/10.1021/jp8039934>.

[70] Y.A. Shaban, S.U.M. Khan, Visible light active carbon modified n-TiO₂ for efficient hydrogen production by photoelectrochemical splitting of water, *International Journal of Hydrogen Energy* 33(4) (2008) 1118-1126. <https://doi.org/10.1016/j.ijhydene.2007.11.026>.

[71] Y. Zheng, G. Chen, Y. Yu, Y. Zhou, F. He, Synthesis of carbon doped WO₃-0.33H₂O hierarchical photocatalyst with improved photocatalytic activity, *Applied Surface Science* 362 (2016) 182-190. <https://doi.org/10.1016/j.apsusc.2015.11.115>.

[72] Y. Park, W. Kim, H. Park, T. Tachikawa, T. Majima, W. Choi, Carbon-doped TiO₂ photocatalyst synthesized without using an external carbon precursor and the visible light activity, *Applied Catalysis B: Environmental* 91(1-2) (2009) 355-361. <https://doi.org/10.1016/j.apcatb.2009.06.001>.

[73] M. Ismael, Latest progress on the key operating parameters affecting the photocatalytic activity of TiO₂-based photocatalysts for hydrogen fuel production: A comprehensive review, *Fuel* 303 (2021). <https://doi.org/10.1016/j.fuel.2021.121207>.

[74] S. Martha, P. Chandra Sahoo, K.M. Parida, An overview on visible light responsive metal oxide based photocatalysts for hydrogen energy production, *RSC Advances* 5(76) (2015) 61535-61553. <https://doi.org/10.1039/c5ra11682a>.

[75] H. Heffner, R. Faccio, I. López-Corral, C-doped TiO₂(B): A density functional theory characterization, *Applied Surface Science* 551 (2021). <https://doi.org/10.1016/j.apsusc.2021.149479>.

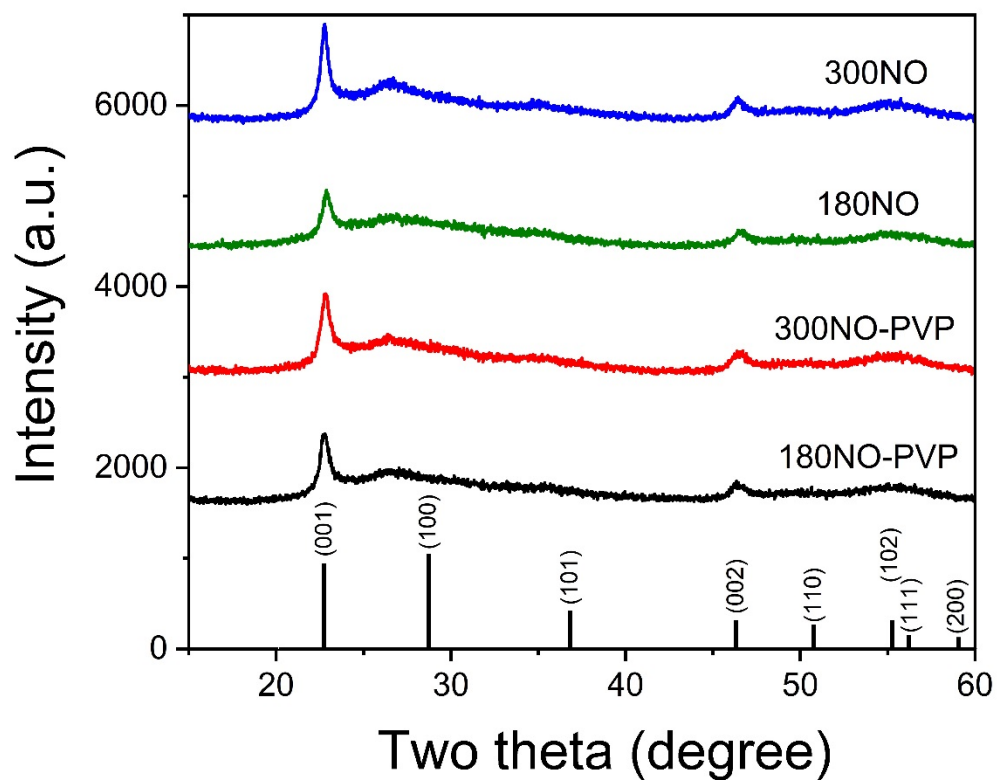


Fig.1. XRD patterns of the samples 180NO (a), 300NO (b), 180NO-PVP (c), and 300NO-PVP (d). The JCPDS card for the pseudo-hexagonal Nb₂O₅ (JCPDS card No. 28-0317) is also shown for comparison.

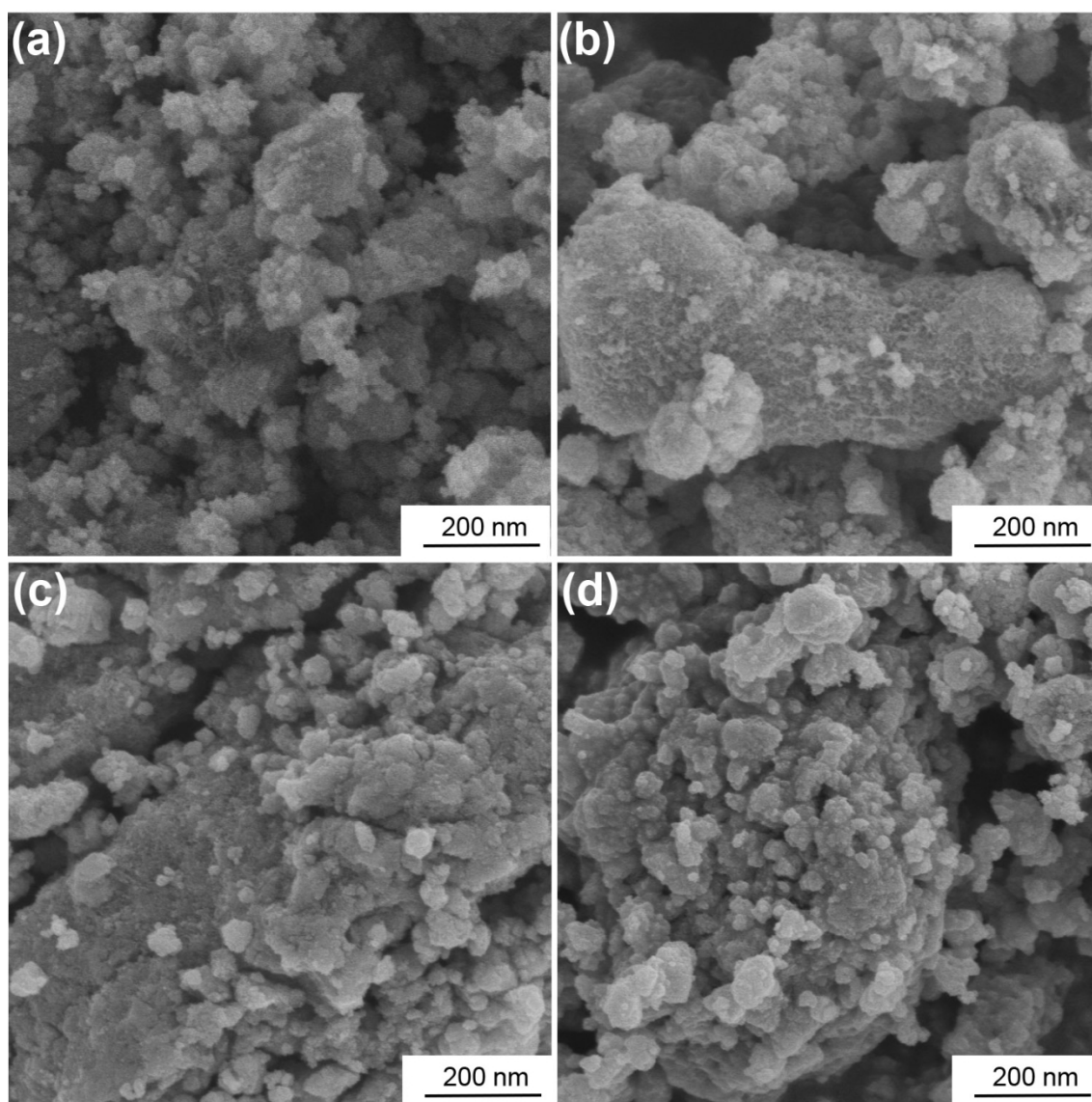


Fig.2. SEM micrographs of the samples 180NO (a), 300NO (b), 180NO-PVP (c), and 300NO-PVP (d).

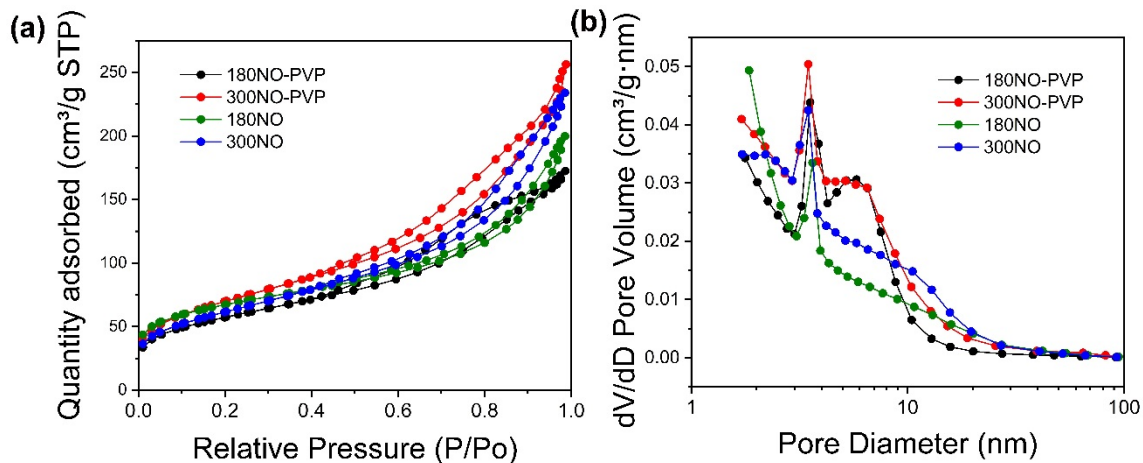


Fig.3. (a) N₂ adsorption/desorption isotherms, and (b) the corresponding pore size distribution curves of 180NO, 300NO, 180NO-PVP, and 300NO-PVP.

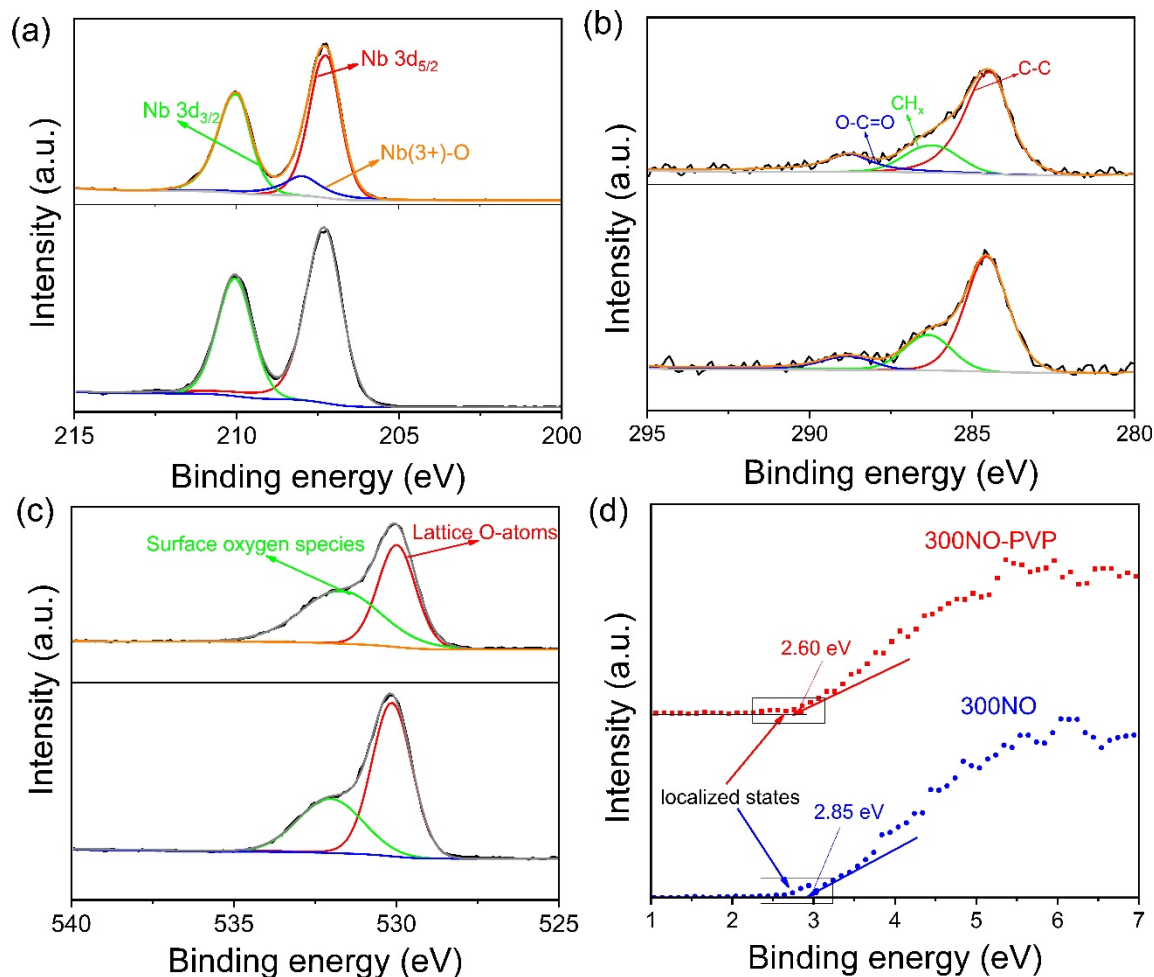


Fig.4. High-resolution XPS spectra comparison of (a) Nb3d, (b) C1s, and (c) O1s peaks between 300NO and 300NO-PVP; (d) valence band XPS curves of 300NO and 300NO-PVP.

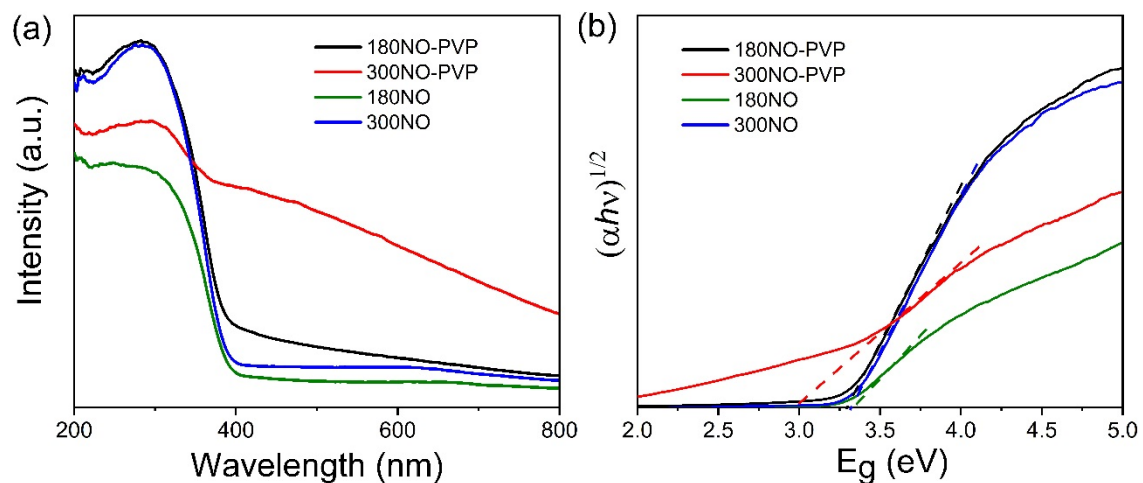


Fig.5. (a) UV-Vis absorption spectra, and (b) calculated bandgaps of 180NO, 300NO, 180NO-PVP and 300NO-PVP.

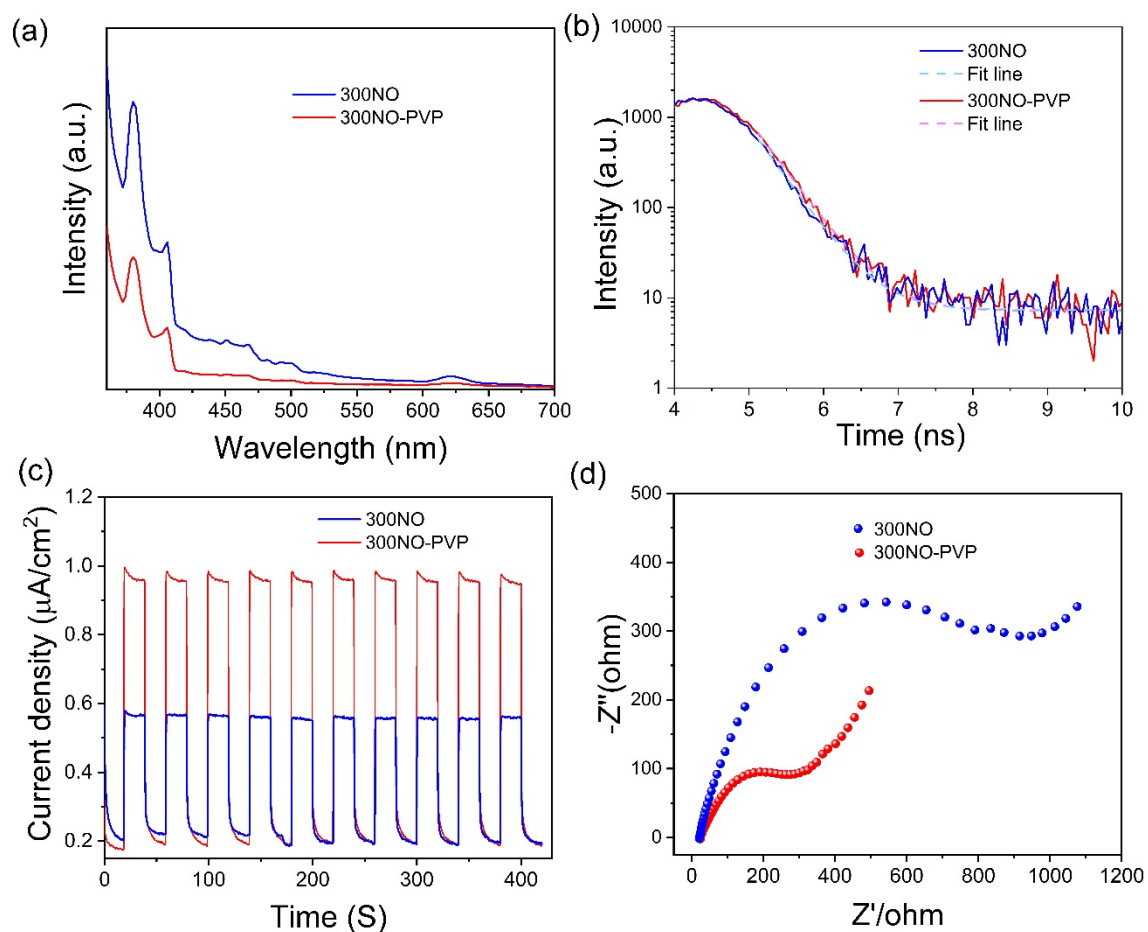


Fig. 6. Photoluminescence spectra (a), and fluorescence emission decay curves (b) of 300NO and 300NO-PVP, excitation at 325 nm; Photocurrent responses (c) and electrochemical impedance spectroscopy (d) of 300NO and 300NO-PVP under visible light irradiation.

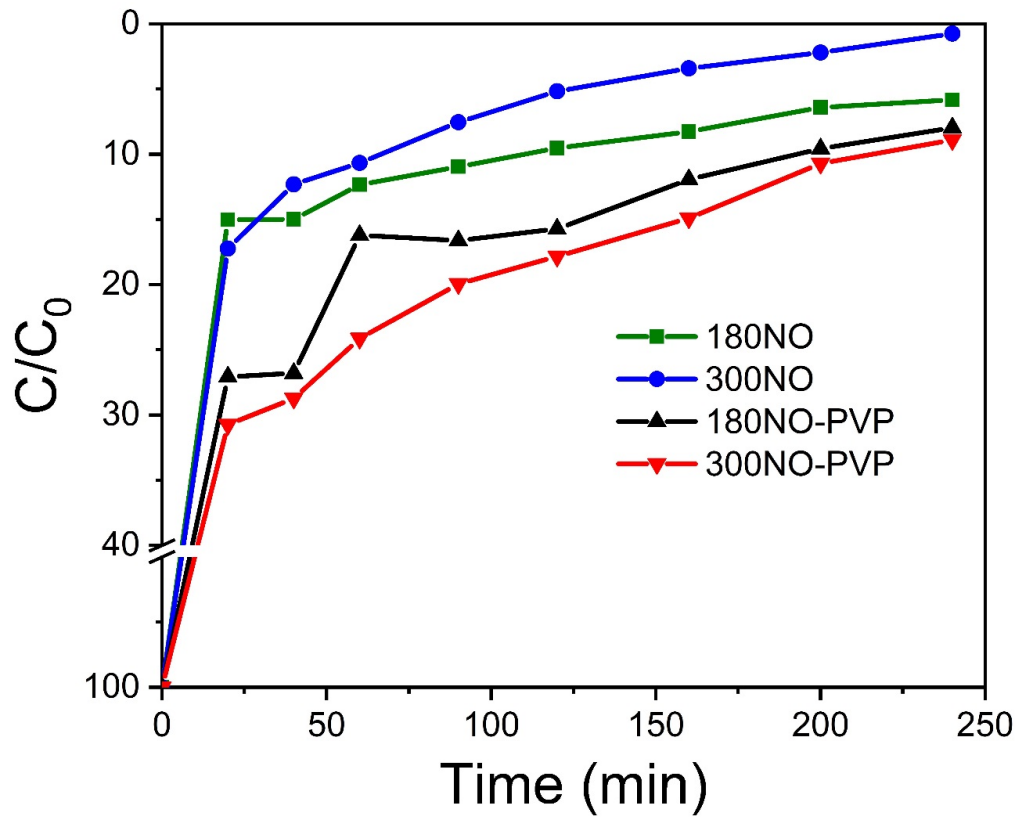


Fig. 7. Adsorption kinetics for MB (initial concentration: 50 ppm) using 180NO, 300NO, 180NO-PVP and 300NO-PVP.

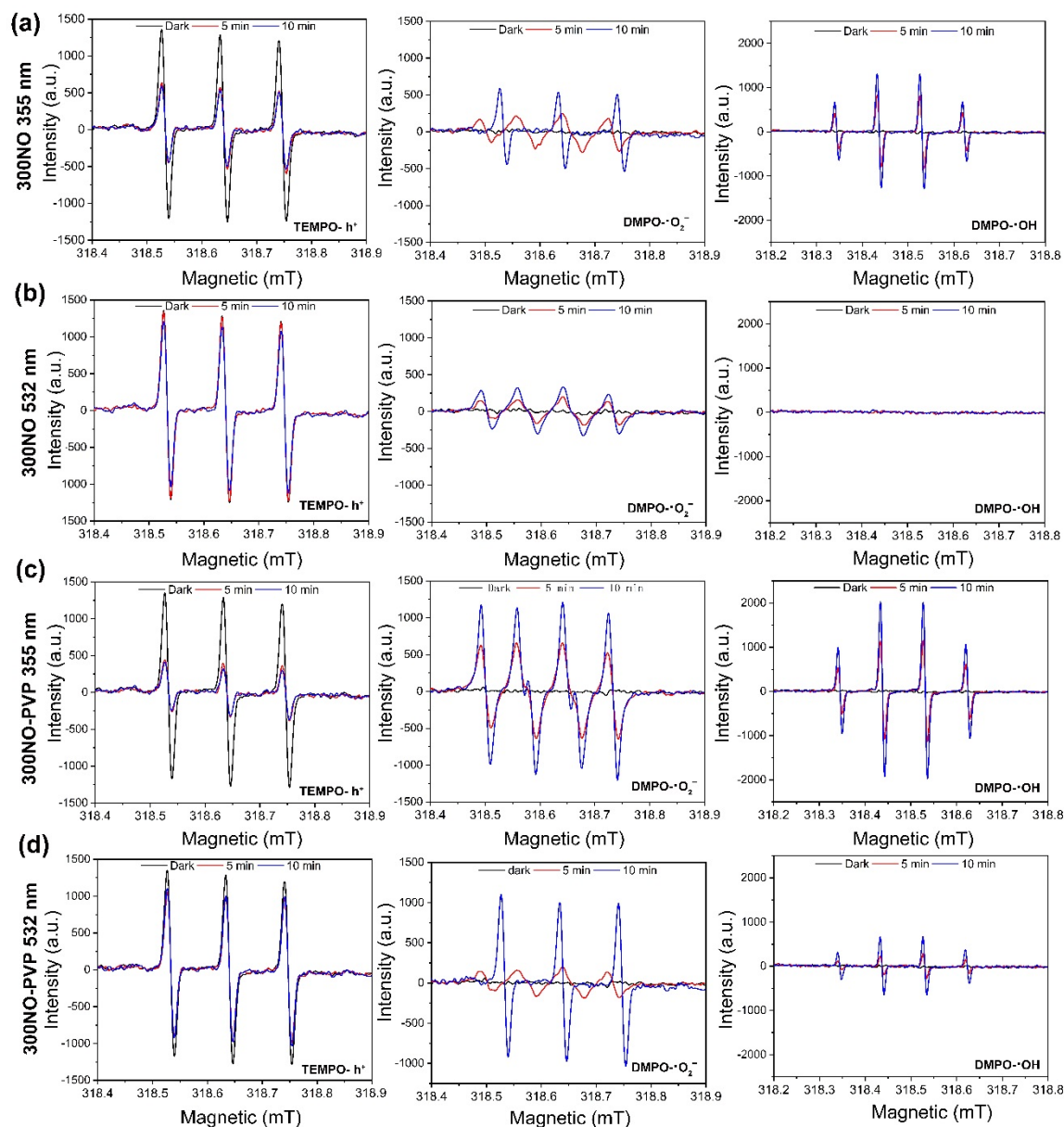


Fig. 8. ESR spectra of the TEMPO-h⁺ adducts, DMPO-OH adducts, and DMPO-O₂⁻ adducts, recorded with 300NO under 355 nm (a) and 532 nm (b) laser irradiation; ESR spectra of the TEMPO-h⁺ adducts, DMPO-OH adducts, and DMPO-O₂⁻ adducts, recorded with 300NO-PVP using 355 nm (c), and 532 nm (d) laser irradiation.

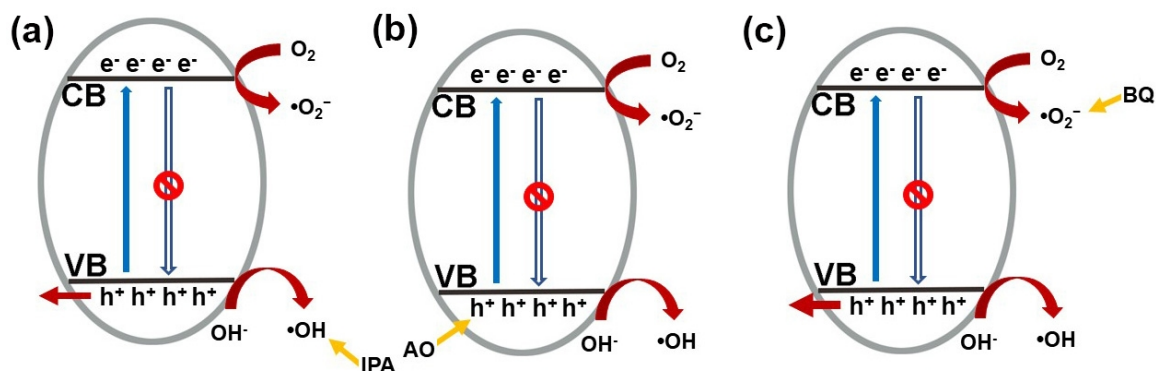


Fig. 9. Proposed charge separation and transportation mechanism for a single-component photocatalyst trapping (a) $\bullet\text{OH}$, (b) h^+ , and (c) $\bullet\text{O}_2^-$ active species. This mechanism is based on the hypothesis that the addition of scavengers can lead to a decrease in electron-hole recombination.

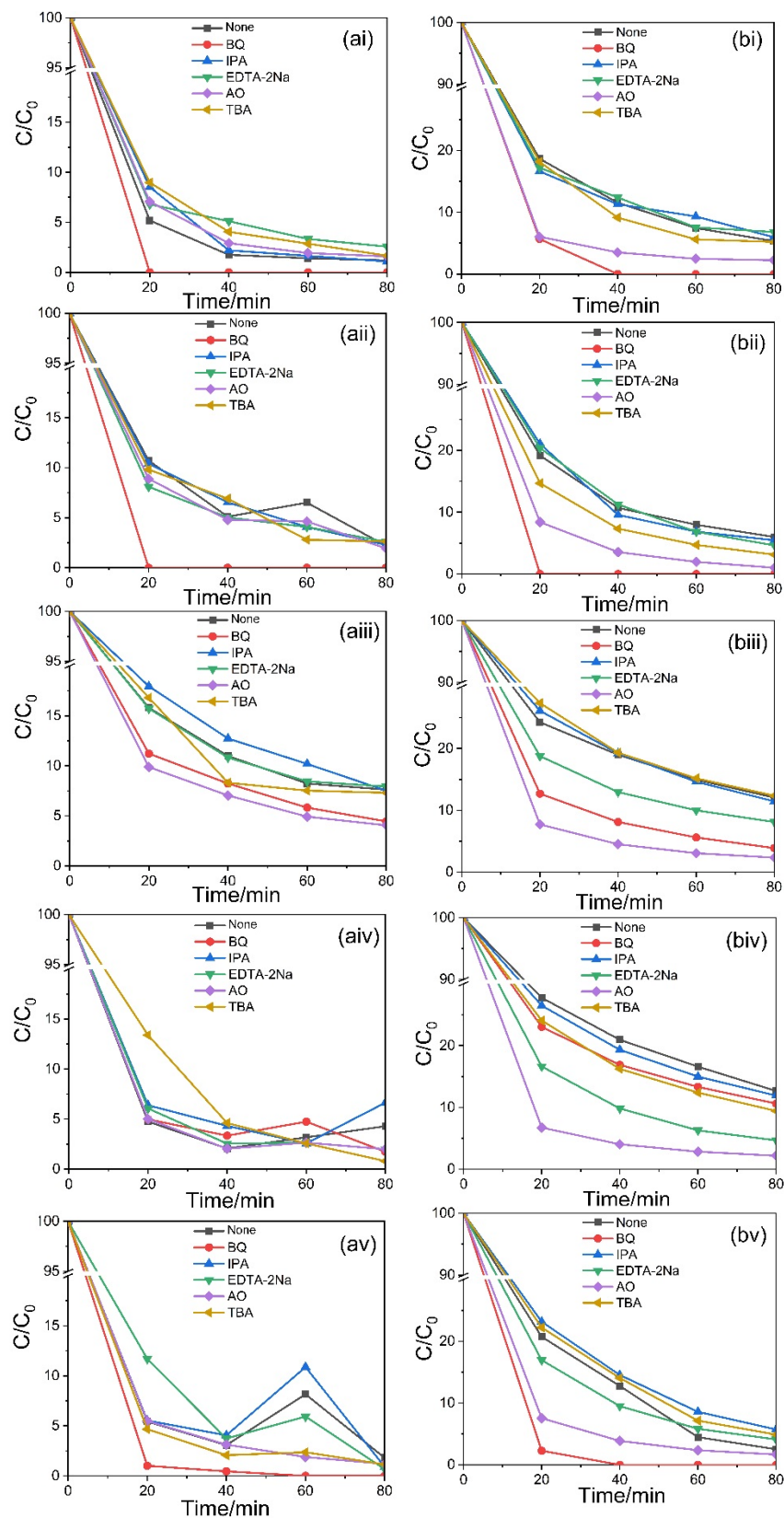


Fig.10. Active-species-trapping experiments using 300NO (a), and 300NO-PVP (b), upon irradiation with 365 nm (i), 420 nm (ii), 535 nm (iii), 630 nm (iv), and white (v) LED lights;

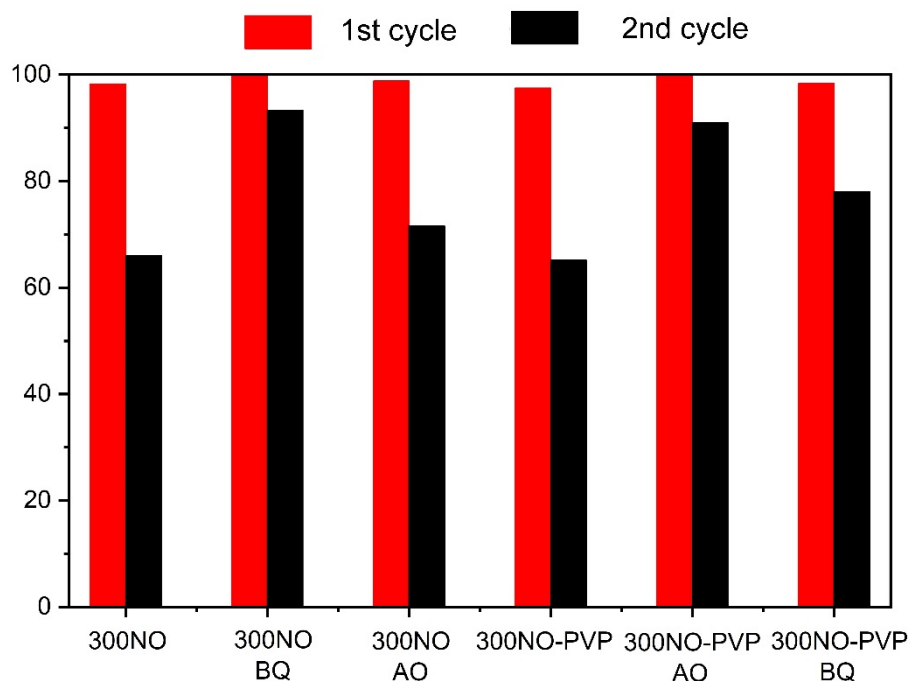


Fig.11. Recyclability of 300NO and 300NO-PVP for the degradation of MB (50 mg/L) and white light irradiation.

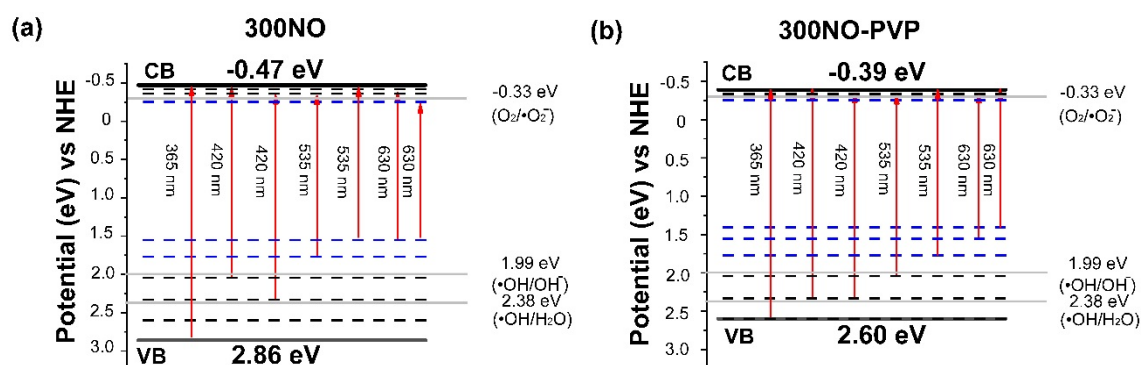


Fig.12. Schematic illustration of the transfer pathway of photogenerated carriers for different energy levels in 300NO (a), and 300NO-PVP (b), at different wavelengths. The dashed lines represent the localized states presented in the forbidden gap.

